Energy & Environmental Science

Cite this: *Energy Environ. Sci.*, 2011, **4**, 4230

www.rsc.org/ees

PAPER

Platinum thin film anodes for solid acid fuel cells

Mary W. Louie[a] and Sossina M. Haile[*ab]

Received 3rd June 2011, Accepted 27th July 2011
DOI: 10.1039/c1ee01889b

Hydrogen electro-oxidation kinetics at the Pt | CsH_2PO_4 interface have been evaluated. Thin films of nanocrystalline platinum 7.5–375 nm thick and 1–19 mm in diameter were sputtered atop polycrystalline discs of the proton-conducting electrolyte, CsH_2PO_4, by shadow-masking. The resulting Pt | CsH_2PO_4 | Pt symmetric cells were studied under uniform H_2-H_2O-Ar atmospheres at temperatures of 225–250 °C using AC impedance spectroscopy. For thick platinum films (>50 nm), electro-oxidation of hydrogen was found to be limited by diffusion of hydrogen through the film, whereas for thinner films, diffusion limitations are relaxed and interfacial effects become increasingly dominant. Extrapolation to vanishing film thickness implies an ultimate interfacial resistivity of 2.2 Ω cm^2, likely reflecting a process at the Pt | $H_{2(g)}$ interface. Films 7.5 nm in thickness displayed a total electro-oxidation resistivity, $\tilde{R}$, of 3.1 Ω cm^2, approaching that of Pt-based composite anodes for solid acid fuel cells (1–2 Ω cm^2). In contrast, the Pt utilization ($\tilde{R}^{-1}$/Pt loading), 19 S mg^{-1}, significantly exceeds that of composite electrodes, indicating that the thin film approach is a promising route for achieving high performance in combination with low platinum loadings.

Introduction

Fuel cells operating at intermediate temperatures are promising alternatives to combustion engines because of their fuel flexibility, high efficiency, and compatibility with inexpensive interconnects. Solid acid fuel cells, in particular, offer the advantage of operation at temperatures near 250 °C using a truly solid electrolyte, CsH_2PO_4, that facilitates anhydrous proton transport with proton conductivities on the order of 10^{-2} S cm^{-1}.[1] Solid acid fuel cells based on thin CsH_2PO_4 electrolyte membranes and Pt composite electrodes have been demonstrated to be viable fuel cells and have been reported to achieve power densities as high as 415 mW cm^{-2} at 248 °C.[2,3] However, the performance of solid acid fuel cells based on platinum electrocatalysts are not yet competitive with those of conventional polymer and solid oxide fuel cells, primarily due to high activation overpotential losses at the electrodes.[4] While it has been possible to fabricate thin electrolyte membranes to improve overall fuel cell performance, achieving electrodes with high activity or competitive platinum loadings remains a challenge.

Elucidation of electrochemical reaction pathways is essential for optimizing electrode microstructure as well as catalyst selection. However, as is the case for a majority of fuel cell systems, the mechanism for electrocatalysis in solid acid fuel cells is not known. Composite electrodes used in operating fuel cells are designed to maximize the number of presumed active sites with the objective of improving electrode performance but are

[a]*Department of Chemical Engineering, California Institute of Technology, Pasadena, CA, 91125*
[b]*Department of Materials Science, California Institute of Technology, Pasadena, CA, 91125*

Broader context

Electrochemical reactions occurring *via* platinum catalysts in solid-state fuel cells have long been considered to proceed at triple-phase boundary sites, where the electrolyte, catalyst and gas phases meet. Therefore, electrodes employed in such fuel cells are typically fabricated from composite (nano)particulate systems to maximize the number of such sites and the total electrochemical current that can flow through the fuel cell. In this work, we explore the reaction pathway for the electrochemical oxidation of hydrogen over platinum thin films in contact with the proton-conducting electrolyte CsH_2PO_4, a system relevant to solid acid fuel cells which operate at a temperature of ~250 °C. We observe that hydrogen oxidation occurs by diffusion of hydrogen through Pt, taking advantage of the entire Pt | CsH_2PO_4 interfacial area rather than being confined to the triple-phase sites. This insight opens up new avenues for developing high performance electrodes with low Pt loadings by freeing the electrode design of the 'tyranny' of the triple-phase boundaries. Indeed, even for flat, planar electrodes of very thin Pt films, we obtain a Pt utilization that is significantly higher than in typical composite electrodes.

not suitable for mechanistic studies because the complex microstructure precludes an unambiguous analysis of the resulting electrochemical response. Consequently, electrode design has progressed *via* trial-and-error without the benefit of rational design rules. In contrast to composite electrodes, electrochemical cells for which the electrode | electrolyte and solid | gas boundaries are well-defined are ideal for studying fundamental electrochemistry in solid state systems. By varying the geometric parameters of the electrode, most conveniently deposited as a patterned, dense thin film, one can examine how the rate-limiting process varies with the number density of candidate active sites, *e.g.*, triple-phase boundary (TPB) and two-phase boundary sites, and ultimately deduce reaction pathways and rate-limiting steps.[5–16] Such an approach is pursued in this work for the study of hydrogen electro-oxidation in CsH_2PO_4-based fuel cells, in which Pt loadings remain prohibitively high.[4] The geometry of interest consists of circular, thin film electrodes which allow access to a wide range of geometric parameters through variation of film diameter and thickness. The resulting Pt | CsH_2PO_4 | Pt symmetric cells were characterized by AC impedance spectroscopy and the rate-limiting step for hydrogen electro-oxidation probed as a function of the electrode dimensions and environmental parameters, specifically, temperature and hydrogen partial pressure.

Experimental

Sample preparation

Dense polycrystalline CsH_2PO_4 discs were fabricated by uniaxial compression of CsH_2PO_4 powders (synthesis detailed elsewhere[5]) at a pressure 138 MPa for 20 min. The discs were mechanically polished with silicon carbide sandpaper (grit sizes 600 followed by 800) and then sonicated in acetone, followed by isopropanol, before drying in air at ~100 °C. The final discs were 19 mm in diameter and ~1 mm thick, with densities 95 ± 2% of theoretical.

Thin film Pt electrodes were deposited onto CsH_2PO_4 discs by DC magnetron sputtering at room temperature using a AJA International ATC Orion system (3 mTorr Ar, 150 W plasma power) or a Cressington 208HR system (~15 mTorr Ar, 80 mA plasma current). Within experimental error, the two deposition systems yielded identical results. The CsH_2PO_4 substrates were shadow-masked to restrict the exposed area to that corresponding to 19, 15, 12.6, 10, 4.7, and 1.3 mm in diameter. The sputtering time was varied to obtain films with thicknesses ranging from 7.5 to 375 nm. The deposition of 10 nm Au films was carried out using the ATC Orion system, with sputtering conditions identical to those for Pt. All cells were fabricated with a symmetric geometry. The fabrication methodology is compatible with the water-soluble nature of the electrolyte, a characteristic that generally precludes patterning based on photolithography.

Characterization

The general crystallinity of the platinum films, adhered to the substrates, was evaluated using a Phillips X'Pert Pro powder X-ray diffractometer using Cu Kα radiation (45 kV, 40 mA) with a 2θ range of 15–90°. Additional analysis was performed using films that were isolated from the substrate. Double-sided tape was applied and the Pt film removed either mechanically or by dissolution of the substrate in water. Diffraction measurements were performed over the 2θ range of 38–42° to access the strongest, (111) peak of Pt, using a step size of 0.008° and various dwell times, depending on the film thickness, to collect sufficient signal intensity for analysis. The full-width half-max of the (111) peak was extracted from a Lorentzian fit and the grain size calculated using the Scherer equation,[17] $t \sim 0.9\lambda/B\cos\theta$, where t is the grain size, $\lambda = 0.1541$ nm, and B is the instrument-corrected full-width half-max at $2\theta \approx 40°$ at which instrument broadening was determined to be ~0.08°.

The morphology of the metal films both before and after electrochemical characterization was observed by scanning electron microscopy, SEM, (LEO 1550VP, Carl Ziess SMT) using a 3 kV accelerating voltage. Film thickness was measured by cross-sectional SEM imaging of fractured cells, and the deposition rate of Pt was determined to be 9.8 nm min^{-1}. Image analysis, specifically, evaluation of the number density of cracks in the films that formed due to thermal cycling, was performed using ImageJ software.[18] The film connectivity was assessed by measuring the sheet resistance of the films, using a hand-held multimeter, both before and after testing.

Impedance spectra were collected, in the majority of cases, using a Solartron Analytical 1260 frequency response analyzer with a 10 mV perturbation voltage about zero bias over frequencies of 10 MHz to 100 mHz configured with a four-probe measurement geometry. For experimental convenience, some spectra were collected using a Solartron 1250 analyzer equipped with a potentiostat (Princeton Applied Research, EG&G 273A). In this case, a three-probe configuration was used, and the high-frequency limit was 60 kHz. For the frequency range of interest, the two instruments yielded excellent agreement in the impedance response. Electrical connection to the cells was made using an in-house constructed sample holder in which the cells were sandwiched between two pieces of Toray carbon fiber paper (280 μm thick) placed between two stainless steel porous discs. Using the sample holder, adequate pressure was applied to the assembly to mechanically contact silver wire leads to the stainless steel discs. The use of carbon fiber paper, with estimated inter-fiber spacings of ~100 μm, ensured sufficient current collection for thin 7.5 nm Pt films. For a subset of the thicker films, electrical connection was made by the direct attachment of silver wires using colloidal silver paint (Ted Pella, #16032); such a method did not yield electrode responses different from that with Toray paper.

Electrochemical impedance measurements were collected under uniform H_2-H_2O-Ar atmospheres at temperatures between 225 and 250 °C. The range of temperatures explored is limited, at one end, by the (reverse) phase transition temperature of ~221 °C on cooling[19] and, at the other end, by the tendency for CsH_2PO_4 to dehydrate at elevated temperatures.[20,21] Hydrogen partial pressures between 0.1 and 0.5 atm, for a fixed water partial pressure of 0.5 atm, were achieved by flowing inlet H_2-Ar mixtures through a heated water bubbler. The water partial pressure of the resulting gas stream was measured with a humidity sensor (HygroFlex 2 with IM 1 probe, Rotronic Instrument Corp). The total gas flow rate of ~160 mL min^{-1} was verified to be sufficiently high so as to eliminate possible mass transport effects, and the perturbation voltage of 10 mV was

confirmed to yield a linear impedance response. Data presented in this work were acquired once the electrode resistance (arc width) exhibited a degradation rate below 2% hr^{-1}.

Acquired impedance spectra were analyzed using the commercial software ZView (Version 2.9b, Scribner Associates, Inc.). In addition to fitting the electrode response, additional circuit elements were placed in series with the electrode circuit to account for contributions from wire resistance, system inductance, and bulk transport properties of the CsH_2PO_4 substrate. The latter, based on the appropriate cell dimensions, was confirmed to yield a proton conductivity value of $2.8 \pm 0.7 \times 10^{-2}$ S cm^{-1} at 250 °C, consistent with the value of 2.4×10^{-2} S cm^{-1} reported in literature.[4] For reasons of clarity and for ease of comparison between spectra, the high-frequency, non-electrode contributions are subtracted from all impedance data presented in this work.

Results and discussion

Film morphology and structure

A typical X-ray diffraction pattern of Pt deposited on CsH_2PO_4 (Fig. 1, 75 nm Pt) shows broad Pt peaks[22] overlaid with monoclinic CsH_2PO_4 peaks.[23] The presence of Pt diffraction peaks, observed even for films as thin as 7.5 nm (not shown), indicates that the deposited film is crystalline in nature, whereas the peak breadth suggests a small grain size.

Representative scanning electron micrographs of Pt on CsH_2PO_4 are shown in Fig. 2. The plane-view image of an as-deposited 75 nm film (Fig. 2a) shows that the Pt conforms to the substrate, revealing the underlying grains of CsH_2PO_4, 0.4–5 μm in size, as well as streaks due to polishing. As evident from the cross-sectional image of a 375 nm film (Fig. 2b), the deposited Pt is formed of nanometric grains and has high density. The film has slightly detached during fracture, giving rise to the small gap at the interface. The conformal and high-density nature of the films (away from the edge) is further evident from Fig. 2c, in which an SEM micrograph of the underside of a 7.5 nm Pt film isolated from its CsH_2PO_4 substrate is shown. As is the case for all films examined, the morphology of the substrate is replicated and the film appears free of pores. While undulation in the film upper surface as a result of the conformal deposition on the uneven substrate is evident in the cross-sectional image, Fig. 2b, the variation in Pt film thickness is estimated, based on deposition on flat substrates, to be less than ± 2%.

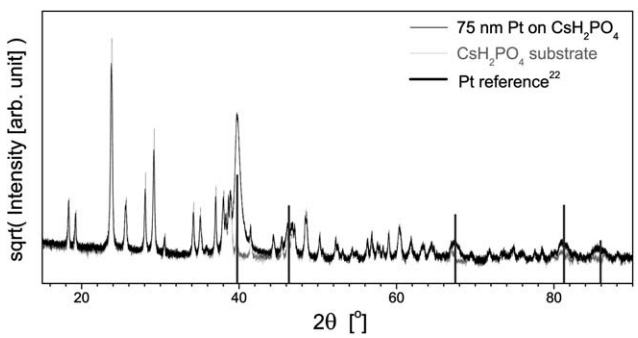

Fig. 1 A representative X-ray diffraction pattern of as-deposited Pt films on a polycrystalline CsH_2PO_4 substrate. Visible are broad Pt peaks, the most prominent at $2\theta = 39.8°$, overlaid with monoclinic CsH_2PO_4 peaks. Pt film shown: 75 nm thick, 15 mm dia.

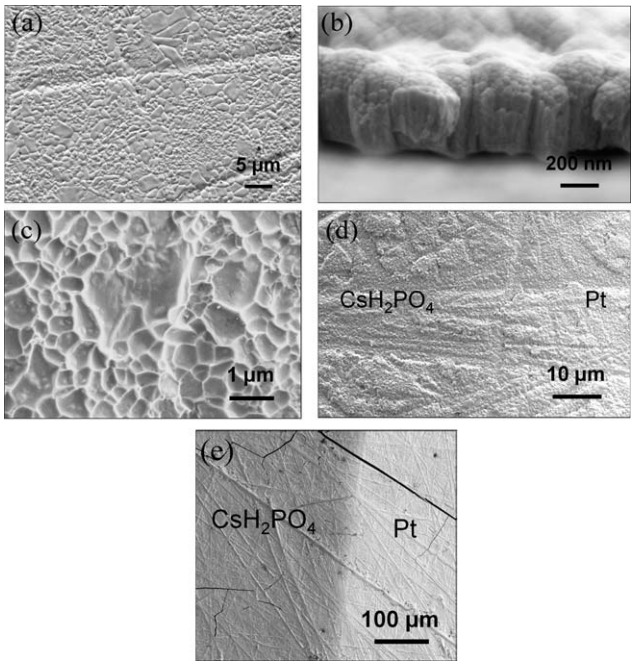

Fig. 2 SEM micrographs of Pt films: (a) as-deposited 75 nm Pt film on CsH_2PO_4, (b) as-deposited 375 nm Pt film in cross-section, (c) underside of as-deposited 7.5 nm film isolated from its substrate, (d) Pt-CsH_2PO_4 boundary for a 375 nm Pt film, and (e) Pt-CsH_2PO_4 boundary for a 375 nm film after electrochemical characterization at 250 °C.

Barring nanoscale porosity, a possibility ruled out below, the morphology of the as-deposited films is ideal for the intended electrochemical study because the TPB sites are limited to the film perimeter region. The boundaries, however, are defined by sloped rather than sharp edges, Fig. 2d, suggesting possible increases to the TPB length relative to an ideal boundary. The slope, spanning 30–50 μm, is so gradual, in fact, that the boundary is barely visible in the high-magnification image. Furthermore, and perhaps more significantly, changes in film structure were observed as a consequence of thermal cycling. The superprotonic transition in CsH_2PO_4 involves a large volume change and structural rearrangement, and this transformation was found to generate microcracks in the electrolyte, which then propagate into the Pt film. The SEM image in Fig. 2e shows a representative image of the boundary region of Pt films on CsH_2PO_4 after thermal cycling. While microcracks were not, in any instance, observed in as-deposited films, cracks of the type evident in the figure were ubiquitous after thermal cycling. It is evident that the features extend from the Pt-free region of the substrate into that on which Pt has been deposited, indicating that the electrolyte is indeed the source of the cracks in the film. The density of TPB sites generated by such cracks is ~0.018 ± 0.004 μm^{-1}, estimated by determining the number and lengths of cracks across ten SEM images. On average, the sheet resistance of the Pt films increased by ~35% after electrochemical measurements, consistent with the formation of microcracks through the film.

Based on observations of the film characteristics, the structure of the gas | Pt | CsH_2PO_4 half cell differs from that expected for a perfectly dense film. Fig. 3 shows a schematic of the structure. The non-ideal features are considered in the evaluation of the electrochemical data.

Fig. 3 A schematic of the Pt | CsH_2PO_4 | Pt cell, with the plane of symmetry denoted by a dashed line. Microcracks, resulting from heating the substrate to above the superprotonic phase transition temperature, are generated in the Pt films.

High-resolution SEM images and diffraction data, Fig. 4 and 5, respectively, indicate that the Pt grain size increases with film thickness. While difficult to quantify from the SEM micrographs, the increasing breadth of the (111) diffraction peak with decreasing film thickness is immediately evident in Fig. 5a, in which the normalized diffraction intensities are compared for a series of films post electrochemical characterization. The particle size implied by the Scherer equation (microstrain effects are considered negligible) is plotted as function of thickness in Fig. 5b. The grain size depends sharply on film thicknesses for films thinner than ~50 nm and then apparently tends towards a finite value with increasing thickness. Selected evaluations of as-deposited films revealed similar grain sizes, indicating that minimal Pt grain growth occurs under the electrochemical characterization conditions (250 °C, total time ~4 days), an expected result.

Electrochemical activity

Effect of platinum film dimensions. Representative impedance spectra collected from the symmetric Pt | CsH_2PO_4 | Pt cells are presented in Fig. 6. For this series of spectra, in which the film diameter is held constant (15 mm) and the film thickness is varied, it is apparent that the nature of the impedance response differs between thick and thin films. Specifically, the thicker films displayed a response in the Nyquist representation (Z_R *vs.* $-Z_I$) that appeared as an asymmetric arc, with a 45° slope at high frequencies and circular appearance at low frequencies. This half-teardrop shape is functionally described by a 'distributed' finite-length Warburg diffusion element, Z_{dFLW}, with impedance

$$Z_{dFLW}(i\omega) = R_0 \frac{\tanh\left[(i\omega\tau)^n\right]}{(i\omega\tau)^n} \quad (1)$$

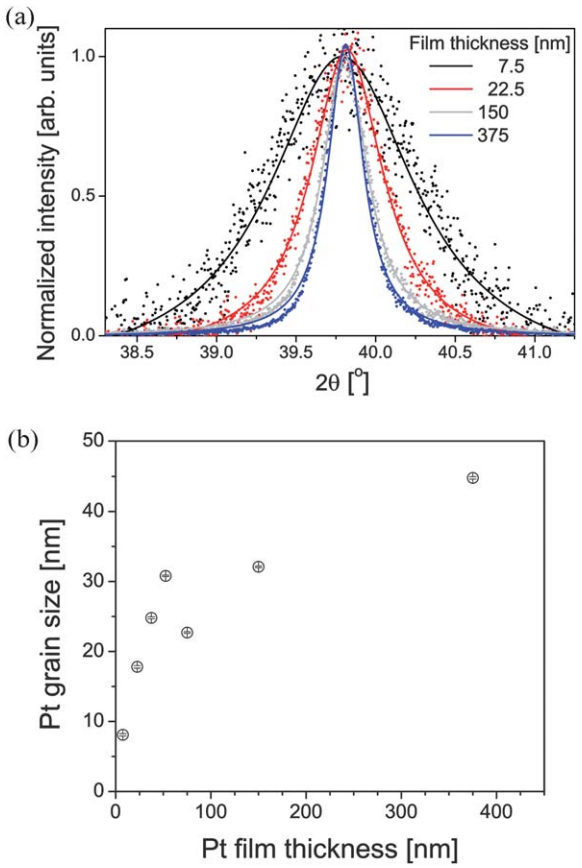

Fig. 5 Correlation of Pt grain size with film thickness: (a) the broadening of the Pt (111) diffraction peak at $2\theta = 39.8°$, shown here for select films, and (b) Pt grain size as a function of film thickness determined from (a). Films measured were isolated from the CsH_2PO_4 substrate (after electrochemical characterization).

where i is $\sqrt{-1}$, ω is angular frequency, τ is the characteristic diffusion time, R_0 corresponds to the real impedance at the low-frequency limit (as indicated in Fig. 6a), and n is a constant whose deviation from 0.5 reflects the dispersion of the response due to non-uniform diffusion.[24] The solid lines in Fig. 6(a–b) show the high quality of the fit using this expression and thus the suitability of this function for representing the measured response. It is further apparent that for thicker films, R_0 increases with film thickness.

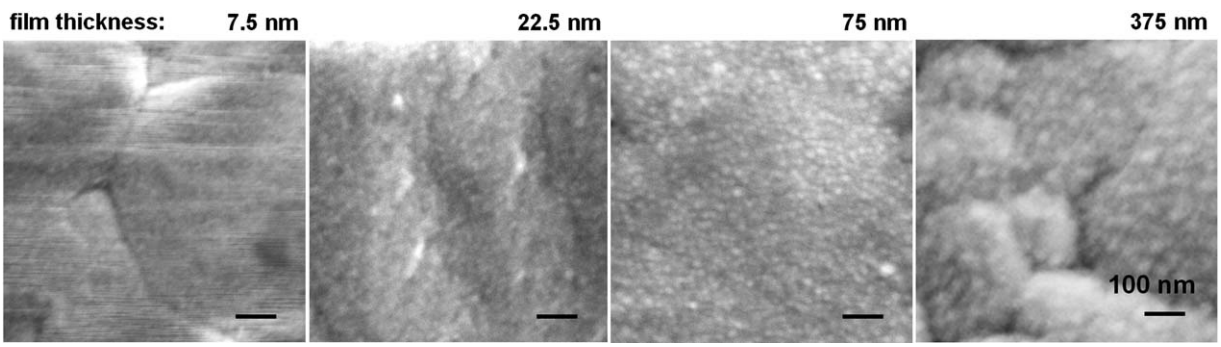

Fig. 4 High-magnification SEM micrographs of Pt films of various thicknesses on top of CsH_2PO_4 (imaged after electrochemical characterization), showing the Pt grain structure.

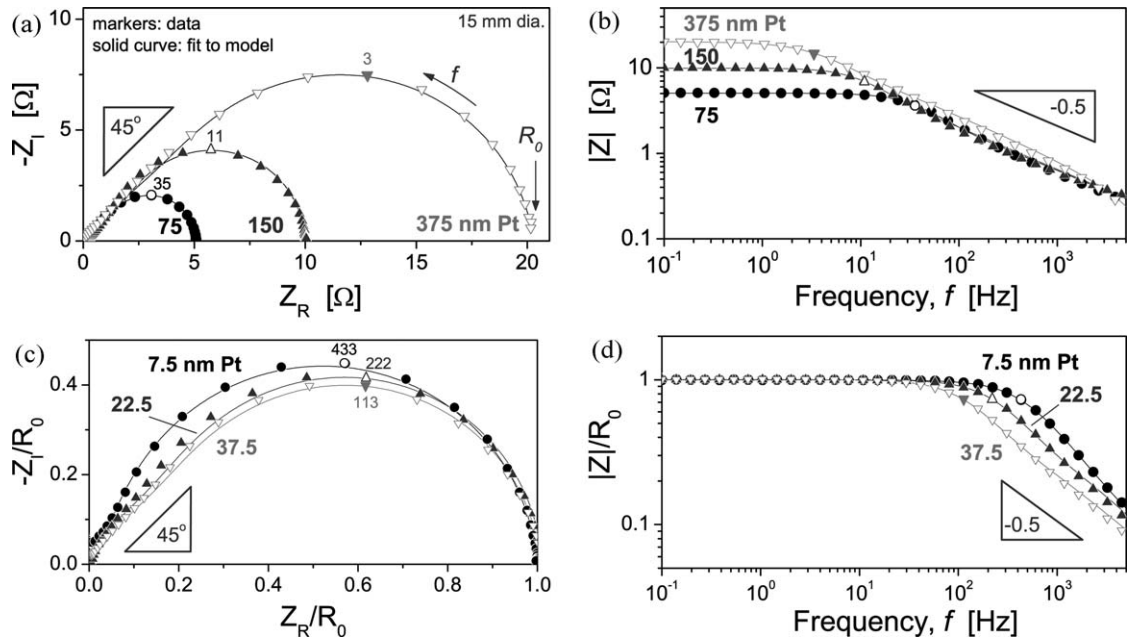

Fig. 6 Impedance spectra for select Pt film electrodes of different thicknesses (15 mm dia.): (a) Nyquist and (b) Bode magnitude representations for thicker films, and (c) Nyquist and (d) Bode magnitude representations of thinner films. Thick Pt films yield a characteristic half-teardrop shape in the Nyquist plot (a), whereas thin Pt films yield a more symmetric response (c). For the thin films (c–d), the impedance response is normalized by the arc width to show the transition in arc shape from half-teardrop to semicircle. Lines indicate fits to the distributed finite-length Warburg element, with the exception of the 7.5 nm Pt film which was fitted using two parallel RQ sub-circuits.

In contrast, the thinner films, Fig. 6(c–d), displayed responses that are not adequately represented by eqn (1). With decreasing film thickness, the electrode arc became increasingly symmetric, and the 45° slope at the high-frequency limit was almost absent for the 7.5 nm film. The solid lines in this case are fits using two parallel RQ sub-circuits, where R is a resistor and Q is a constant phase element ($Z_Q = 1/Y_Q(i\omega)^n$, with Y_Q is a constant and $0 \leq n \leq 1$), placed in series with one another. For ease of comparison of the shapes, the spectra are presented in normalized form.

The characteristics represented by the spectra for 15 mm diameter Pt films in Fig. 6 were observed to be independent of film diameter. That is, irrespective of diameter, all films with thickness ≥50 nm displayed the type of response shown in Fig. 6(a–b), whereas thinner films showed increasingly symmetric arcs, as shown in Fig. 6(c–d). For either type of response, it is possible to evaluate the real impedance of the electrode in the DC limit, explicitly noted as R_0, in Fig. 6a. The results are summarized in Fig. 7, in which R_0 is plotted in double-logarithmic form as a function of film thickness (Fig. 7a) and of film diameter (Fig. 7b). The trends shown in Fig. 7a reflect a clear differentiation between regimes. For thicker films (Regime I), which exhibited the half-teardrop response, the double-logarithmic plot displays an average slope of 0.9 ± 0.1, revealing that R_0 scales linearly with thickness. Thinner films (Regime II), in contrast, tend towards an apparently limiting value of R_0, with further reductions in film thickness having decreasing impact. It is noted that reliable impedance measurements could not be made using films thinner than 7.5 nm because of loss of connectivity in the film during electrochemical characterization. Turning to the diameter dependence of R_0 (Fig. 7b), it is evident that for all films, the data fall along a line with an average slope of -2.1 ± 0.1, indicating that R_0 is inversely proportional to the area of the Pt film.

The behavior of R_0 as a function of temperature and hydrogen partial pressure (Fig. 8) further suggests a mechanistic distinction between thicker (Regime I) and thinner (Regime II) films. Specifically, the reaction order for pH_2 (*i.e.*, r in $R_0^{-1} \propto pH_2^r$) is roughly constant at ~0.4 for thicker Pt films (Regime I) but increases sharply with decreasing film thickness (Regime II), attaining a value of ~0.75 for 7.5 nm films. Likewise, the activation energy for R_0^{-1} is somewhat flat in Regime I, with a value of ~42 kJ mol^{-1} for film thicknesses ≥150 nm and decreasing with decreasing film thickness to ~27 kJ mol^{-1} at 7.5 nm.

The combination of the observed film dimension (thickness and area) dependences of both the absolute value of R_0 and the form of the impedance response can be interpreted as follows. In all cases examined, the rate-limiting step occurs at sites that scale in number density with film area. For thicker films, diffusion to access these sites is rate-limiting, giving rise to the linear dependence of R_0 on film thickness and the characteristic half-teardrop shape of the impedance response. For thinner films, diffusion no longer plays a role in limiting the rate of the process, however, the pathway continues to involve sites distributed through the film area. For truly dense films, one could readily conclude from these results that, for the range of film dimensions examined, triple-phase boundaries do not contribute to the measured electrochemical activity. Even the sloped, irregular film boundaries do not create a significant concentration of active sites as this would lead to a diameter rather than area dependence of the overall activity. Because the extent of the sloped region is no more than 50 μm, it amounts to less than 8% of the total film area of even the smallest diameter films, and thus, the minimal role of these sloped boundaries can be understood. However, the existence of cracks throughout the films that cause an increase in the TPB site density in a manner that scales with film area precludes

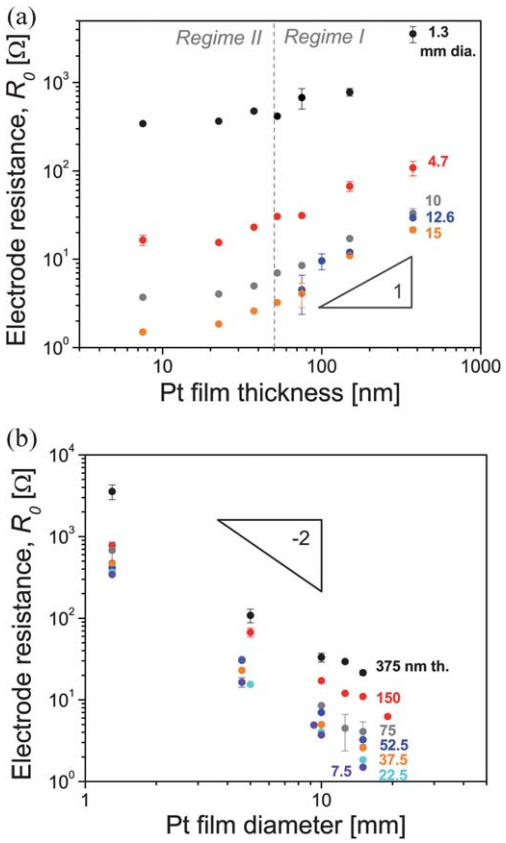

Fig. 7 Double-logarithmic plots of the Pt film electrode resistance, R_0, as a function of: (a) film thickness for various diameters and (b) film diameter for various thicknesses. The shapes of the impedance spectra (Fig. 6) reveal two different regimes: for thicker Pt films, the impedance response yields a half-teardrop shape, whereas for thinner films, the spectra become increasingly symmetric. The change in shape of the impedance response coincides with a change in slope in (a) from 1 for thicker films to a smaller value for thinner films. The slope of −2 in (b) indicates that for all Pt films, R_0 scales with film area.

a definitive conclusion simply based on film dimension arguments. Similarly, possible nanoscale porosity in the films enabling gas access to TPB sites at the Pt | CsH_2PO_4 interface

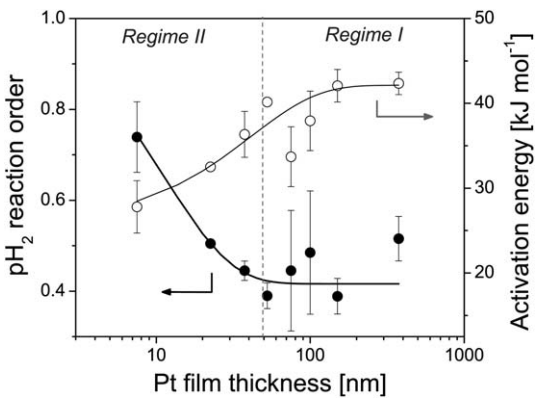

Fig. 8 Plot of the pH_2 reaction order and the activation energy of the electrode process as a function of film thickness, consistent with a change in the rate-limiting step with film thickness. Solid lines serve as guides to the eye.

Fig. 9 A schematic of the Au | Pt | CsH_2PO_4 | Pt | Au symmetric cell, with the plane of symmetry denoted by a dashed line. Microcracks, resulting from heating the substrate to above the superprotonic phase transition temperature, are propagated to the Pt | Au film.

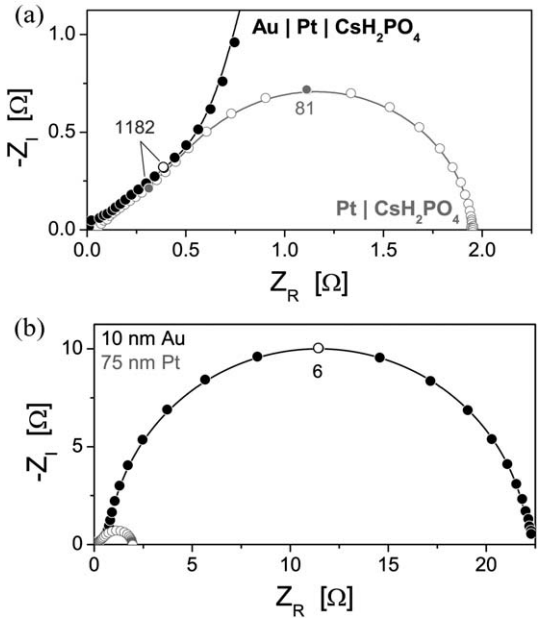

Fig. 10 Comparison of electrode responses from Au | Pt | CsH_2PO_4 | Pt | Au and Pt | CsH_2PO_4 | Pt symmetric cells (15 mm dia. films, 10 nm Au, 75 nm Pt): (a) At high frequencies, both spectra overlap and exhibit a phase angle of 45°, while (b) at lower frequencies, the behavior the Au | Pt cell deviates significantly from that of the Pt cell.

could be expected to yield dependences on film dimensions in a manner similar to that observed here. To address this ambiguity, we turn to the results obtained from cells in which Au was applied atop the Pt films.

Impact of Au overlayers. SEM imaging of Au | Pt films with ~10 nm Au deposited on 75 nm Pt (not shown) revealed that the bilayer films attained morphologies essentially identical to those with Pt only (*e.g.*, Fig. 2). That is, the as-deposited films were crack-free, but after a thermal cycle microcracks were evident throughout the film area. Given that the cracks formed after Au deposition, all triple-phase boundaries generated as a result of cracking are taken to be free of Au and thus equally active as those formed in the absence of Au. The inferred geometry is presented in Fig. 9.

A comparison of the impedance responses for samples (75 nm Pt) with and without an Au overlayer (10 nm Au) reveals the dramatic impact of changing the nature of the exposed metal surface on the overall reaction impedance, Fig. 10. The two spectra overlap almost perfectly at high frequencies ($f > 600$ Hz) at which the spectra are linear with a 45° slope in the Nyquist representation (Fig. 10a). They deviate substantially at intermediate and especially low frequencies, and the DC electrode

resistance is over an order of magnitude higher in the presence of Au (Fig. 10b). The retention of the linear, 45° phase angle response at high frequencies upon deposition of Au is evidence that the diffusive process is retained. The dramatic increase in the absolute resistance at low frequency, on the other hand, reveals that the overall electrochemical reaction pathway must involve a step at the Pt | Au | H_2 interfaces, and hence in the absence of Au must proceed *via* the Pt | H_2 interface. That is, the diffusion step must occur in serial with a step at these interfaces, where the interfacial step(s) become(s) extremely slow in the presence of Au. These results thus rule out the possibility that TPBs generated by cracking play any significant role on the electro-oxidation of hydrogen for the film geometries employed here. Similarly, in the absence of an unusual situation in which a ~10 nm thin film of Au closes possible linear pores in a 75 nm Pt film, these results also rule out diffusion through nanoscale pores as a possible pathway for hydrogen electro-oxidation.

Diffusion analysis. With bulk diffusion through Pt having been revealed as the rate-limiting step for thicker films, the impedance data can be used for the determination of diffusion parameters. Specifically, the impedance response for the diffusion of a neutral species through a medium bounded by reversible planes/electrodes[25] has the form given in eqn (1), with $n = 0.5$ and $\tau = L_F^2/\tilde{D}$, where L_F is the film thickness and $\tilde{D}$ is the (ambipolar) diffusion coefficient of a neutral species, taken here to be interstitial hydrogen (irrespective of possible dissociation into protons and electrons or into hydride ions and holes).[26,27] When the solution furthermore behaves ideally (dilute solution limit), the resistance in the DC limit is given by

$$R_0 = \frac{k_B T}{e^2 D_H c_H} \frac{L_F}{A_F} \quad (2)$$

where k_B, T and e have their usual meanings, c_H is the concentration of hydrogen in the Pt film, and A_F is the film area. An absolute valence of 1 is assigned to the transported species which is ultimately incorporated as protons at the Pt | CsH_2PO_4 interface. Although n in eqn (1) is strictly 0.5 for a finite-length Warburg diffusion response, treating it as a fitted parameter, as was done here, provides an indication of microstructural imperfections/variations present in the films. Across 44 samples, n ranged from 0.41 to 0.58 with an average value of 0.48 ± 0.03, a relatively small deviation from 0.5. Moreover, no correlation between n and any obvious experimental conditions or parameters was observed, suggesting that random sample-to-sample variations in film structure are responsible for the slight scatter.

Analysis of the impedance data of 44 symmetric cells in the manner described above yielded hydrogen diffusion coefficients (D_H) and concentrations (c_H) on the order of 10^{-12} m^2 s^{-1} and 10^{-4} H/Pt, respectively, Table 1. Over the relatively narrow temperature window explored, c_H was largely unchanged, whereas from the temperature dependence of D_H an activation energy of 47 ± 6 kJ mol^{-1} was determined. It is not possible to directly compare these values to those in the literature because all other reported studies address different temperature ranges. Extrapolation of literature values[28–31] to the temperatures examined here suggest a hydrogen diffusion coefficient in the range of 10^{-12} to 10^{-9} m^2 s^{-1} and a concentration in the range 10^{-8}–10^{-4} H/Pt. The present values, though apparently reflecting low diffusivity and high solubility, lie within these ranges and are physically realistic. Reported activation energies for Pt[28–31] are between 25 and 40 kJ mol^{-1}, the wide scatter likely being a consequence of the low solubility of hydrogen in this metal. While the value measured here, 47 ± 6 kJ mol^{-1}, is somewhat high relative to this range, given the uncertainty in the literature data and the atypical temperature regime of the present study, it is reasonable to accept that the measurement reflects the same general type of process.

Beyond the expected temperature dependence of D_H, an unexpected dependence on film thickness was observed, Fig. 11. Notably, c_H displayed an approximately inverted dependence on film thickness such that the product $D_H \times c_H$ remained approximately constant (not shown). Given the dependence of average Pt grain size on film thickness, Fig. 4 and 5, such behavior immediately suggests that the hydrogen transport mechanism depends on microstructure in a systematic manner. Specifically, the combination of somewhat high activation energy for hydrogen transport, low value of D_H, and microstructure dependence all suggest bulk diffusion through the films with grain boundaries as trapping sites. More significant in the present context than the details of hydrogen transport through Pt is the fact that the absolute values of D_H and c_H support the surprising conclusion that the hydrogen electro-oxidation pathway involves hydrogen diffusion through the bulk of the films. Thus, for the range of film dimensions explored, the process is limited by the quantity of two-phase boundary sites (either Pt | gas or Pt | CsH_2PO_4) rather than the quantity of triple-phase boundary sites.

Ultra-thin Pt films. For the thinnest films for which reliable data could be obtained (7.5 nm), the change in the features of the impedance response from those of thicker films is most certainly due to a change in the nature of the rate-limiting step. As the transport distance is decreased, diffusion limitations are relaxed, and interfacial effects at either or both the Pt | gas and Pt | CsH_2PO_4 boundaries become rate-limiting. In the absence of transport of a neutral species as the dominant response, the impedance response is expected to adopt a characteristic symmetric shape in the Nyquist representation, and the Z_{dFLW} element becomes inadequate for representing the response. For convenience, an equivalent circuit with two parallel RQ sub-circuits placed in series with one another was used to analyze the data, as shown in Fig. 6(c–d). From this analysis, we find the total electrode resistivity (area-normalized resistance) across twelve different samples, to have a value of 3.1 ± 0.5 Ω cm^2.

For the serial set of steps suggested by this analysis, the total resistivity, $\tilde{R}$, is expected to be the simple sum of the interfacial

Table 1 Experimentally determined parameters for hydrogen transport in Pt, shown for two temperatures. Values reported are taken from averaging over films greater than 50 nm in thickness

T [°C]	D_H [× 10^{-12} m^2 s^{-1}]	c_H [× 10^{-4} H/Pt]
250	1.6 ± 0.7	2.4 ± 0.8
225	0.9 ± 0.5	2.8 ± 0.8

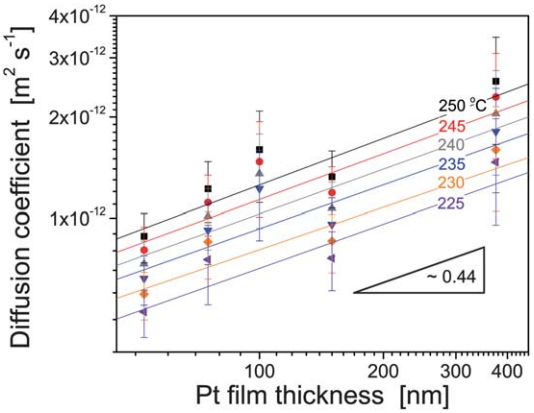

Fig. 11 A plot of the extracted hydrogen diffusion coefficient as a function of Pt film thickness for several temperatures. Error bars indicate the scatter of the value over several samples. Linear fits to each data set yield slopes with an average value of 0.44.

reaction resistivity, $\tilde{R}_{rxn}$, and the thickness-dependent resistivity due to diffusion, $\tilde{R}^*_D L_F$:

$$\tilde{R} = \tilde{R}_{rxn} + \tilde{R}^*_D L_F \quad (3)$$

The area-normalized data from Fig. 7a indeed collapse into a single curve, Fig. 12, which, in double-logarithmic format, display the expected flat regime at small film thickness and regime of slope 1 at large film thickness. The fit to eqn (3), also shown in the figure, implies $\tilde{R}_{rxn} = 2.2\ \Omega\ cm^2$ and $\tilde{R}^*_D = 0.081\ \Omega\ cm^2\ nm^{-1}$. For the thinnest film that could be evaluated (7.5 nm) with a total electrode resistivity of $3.1 \pm 0.5\ \Omega\ cm^2$, the diffusion contribution is $0.9\ \Omega\ cm^2$, or approximately 27% of the total. Thus, both interfacial and bulk effects play a role even in very thin films.

Implications for electrode design

Platinum is known to display relatively poor hydrogen permeation characteristics and accordingly was not anticipated to facilitate hydrogen electro-oxidation *via* a bulk diffusion pathway. The dominance of the two-phase boundary pathway over the TPB pathway results, in part, from the thin film geometry employed, which maximizes the Pt | CsH_2PO_4 interfacial area while minimizing the number of TPB sites. In principle, the TPB activity would be accessed by increasing the thickness of platinum until the two-phase boundary pathway, governed by hydrogen diffusion through the film, is effectively blocked. However, because physical shadow masks are limited to relatively large areas (the smallest diameter used here was 1 mm), unrealistically thick films of Pt would be needed. An estimate of the lower bound for the resistivity of the TPB pathway is instead made using impedance data acquired from electrode films with configurations similar to that shown in Fig. 9. Specifically, blocking studies with 50 nm Au films yielded electrode resistivities as high as $225\ \Omega\ cm^2$, while retaining diffusion characteristics at high frequencies of the type evident in Fig. 10. The shape of the spectra implies that even with such extreme resistance in the blocking layers, the TPB pathway is not favorable and can be used to establish the maximum activity of TPB sites. Based on a TPB density of $\sim 180\ cm^{-1}$, the lower bound for the TPB resistivity is estimated at $\sim 41\ k\Omega$ cm.

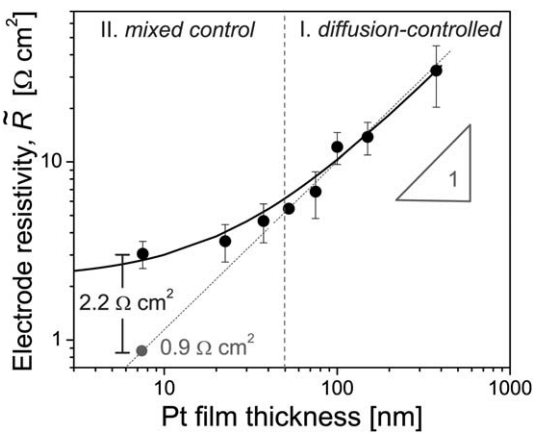

Fig. 12 Electrode resistivity plotted against film thickness for all Pt | CsH_2PO_4 | Pt cells tested in this study. The solid curve corresponds to eqn (3), and the surface resistivity was determined by extrapolation of the resistivity due to diffusion to a Pt film thickness of 7.5 nm (dotted line).

Irrespective of the absolute resistivity values, one can expect the triple-phase boundary pathway to overtake the two-phase boundary pathway for Pt dimensions (diameter and thickness) which provide sufficient triple-phase site density relative to the two-phase interfacial area. One can speculate that a continuous Pt film with nanometric pores would lead to maximum overall activity. For a two-phase boundary resistivity of $3.1\ \Omega\ cm^2$ and a minimum TPB resistivity of 41 kΩ cm, an area-to-perimeter ratio of ~7.6 μm or less is required to observe comparable total activity between two-phase and triple-phase boundary sites in 7.5 nm films. While eventual fabrication of such structures could likely be achieved, because of the uncertainty with respect to the TPB site activity, there is no guarantee that such electrodes would, in fact, provide higher activity than the dense films examined here. Furthermore, pore-free films provide the inherent advantages of high electronic conductivity and good thermal stability.

These factors prompt a direct comparison of the activity of dense Pt thin films to state-of-the-art composite electrodes employed in solid acid fuel cells, Table 2. The absolute (area-normalized) resistivity of the 7.5 nm film is within a factor of two of that of composite electrodes formed solely of nanoparticulate Pt and CsH_2PO_4. Specifically, electrodes fabricated by electrospray deposition[32] and by mechanical mixing[33] yield comparable resistivity values of 1.5 and $1.7\ \Omega\ cm^2$, respectively. Pre-commercial solid acid fuel cells, in which Pt/C is also an electrode component and thus take advantage of carbon to enhance electronic conductivity, have much smaller electrode resistivities, just $0.06\ \Omega\ cm^2$.[4] Although the thin film Pt electrode displays the highest resistivity, the amount of Pt applied is the lowest (by a factor of 10–500 in mass) such that the Pt utilization or mass-normalized activity ($\tilde{R}^{-1}$/Pt loading) is the highest, 19 S mg^{-1}. The poor activity in the nanoparticulate cases suggests a large fraction of the Pt is not utilized because of the lack of electronic connectivity. The results further suggest that increasing the overall electrode activity can be increased simply by increasing the projected Pt | CsH_2PO_4 contact area. Promising results taking advantage of precisely such an electrode geometry, albeit targeting the cathode, have

Table 2 Comparison of platinum-based anodes for solid acid fuel cells at temperatures of 238–250 °C

Electrodes	Electrode resistivity [Ω cm²]	Pt loading [mg cm⁻²]	Mass-normalized activity [S mg⁻¹]
7.5 nm Pt film – *sputtered* (*this work*)	3.1 ± 0.5	0.017	19
Pt:CsH_2PO_4 (1 : 2) – *electrosprayed*[32]	1.5	0.3	2.2
Pt:CsH_2PO_4 (1 : 2) – *mech. mix.*[33]	1.7	10	0.059
Pt:Pt/C:CsH_2PO_4 (3 : 1 : 3) – *mech. mix.*[2,4]	0.06	7.7	2.2

been recently reported.[3,34] In that work, a uniform Pt coating is applied to sub-micron CsH_2PO_4 powders using a metal-organic chemical vapor deposition method.[34] A decrease in the CsH_2PO_4 particle size led to a monotonic decrease in electrode resistance,[3] indicating the importance of the total Pt | CsH_2PO_4 surface area. Using such techniques, one can readily envision a substantial increase in specific surface area over that of a flat interface, and from the quantitative studies reported here, the impact on performance metrics can be assessed. For CsH_2PO_4 particle-based electrodes of moderate thickness, we presume the activity will scale linearly with surface area, and thus, a 50-fold increase in the specific surface area, for example, will decrease the electrode resistivity to a highly attractive value of $\sim 0.06\ \Omega\ cm^2$ for the 7.5 nm thick film. The Pt loading will also increase proportionally, but would remain at just 0.86 mg cm^{-2}. Thus, thin, continuous film electrodes have the potential to dramatically reduce Pt loadings while also enhancing power output.

Conclusions

The rate-limiting step for hydrogen electro-oxidation over Pt thin film electrodes has been identified. Pt films between 7.5 and 375 nm thick were determined to electrocatalytically oxidize hydrogen *via* the two-phase boundary pathway. Pt films greater than 50 nm in thickness are rate-limited by diffusion of hydrogen through the film, whereas for films thinner than 50 nm, interfacial processes, with a resistivity of 2.2 Ω cm^2, become increasingly important as the rate-limiting step. That the two-phase boundary pathway is preferred over the triple-phase boundary pathway has significant implications for the design of electrodes in solid acid fuel cells. Specifically, electrodes based on 7.5 nm Pt films with electrode resistivities of 3.1 Ω cm^2 have the potential to reach state-of-the-art performances while using one order of magnitude less Pt by mass. This improvement is a consequence of the inherent interconnectivity of the platinum in the thin film configuration and the resulting improvement in catalyst utilization compared to conventional electrodes based on Pt nanoparticles.

Acknowledgements

This material is based upon work supported by the National Science Foundation under Grants No. DMR-0906543 and DMR-0520565. Funding was also provided by the Gordon and Betty Moore Foundation through the Caltech Center for Sustainable Energy Research. M. W. Louie was supported in part through the NSF Graduate Research Fellowship Program. The authors thank William Chueh for programming assistance and Calum Chisholm and Yoshihiro Yamazaki for valuable discussion.

References

1 D. A. Boysen, T. Uda, C. R. I. Chisholm and S. M. Haile, *Science*, 2004, **303**, 68.
2 T. Uda and S. M. Haile, *Electrochem. Solid-State Lett.*, 2005, **8**, A245.
3 C. R. I. Chisholm, D. A. Boysen, A. B. Papandrew, S. Zecevic, S. Cha, K. A. Sasaki, A. Varga, K. P. Giapis and S. M. Haile, in *Interface*, The Electrochemical Society, New Jersey, 2009, vol. 18, ch. 53, pp. 53–59.
4 S. M. Haile, C. R. I. Chisholm, K. Sasaki, D. A. Boysen and T. Uda, *Faraday Discuss.*, 2007, **134**, 17.
5 M. W. Louie, K. Sasaki and S. M. Haile, *Electrochem. Soc. Trans.*, 2008, **13**, 57.
6 J. Fleig, *Solid State Ionics*, 2003, **161**, 279.
7 F. S. Baumann, J. Fleig, H. U. Habermeier and J. Maier, *Solid State Ionics*, 2006, **177**, 1071.
8 R. O'Hayre and F. B. Prinz, *J. Electrochem. Soc.*, 2004, **151**, A756.
9 W. C. Chueh and S. M. Haile, *Phys. Chem. Chem. Phys.*, 2009, **11**, 8144.
10 G. J. la O' and Y. Shao-Horn, *J. Electrochem. Soc.*, 2009, **156**, B816.
11 W. Jung and H. L. Tuller, *J. Electrochem. Soc.*, 2008, **155**, B1194.
12 A. Bieberle, L. P. Meier and L. J. Gauckler, *J. Electrochem. Soc.*, 2001, **148**, A646.
13 J. Mizusaki, K. Amano, S. Yamauchi and K. Fueki, *Solid State Ionics*, 1987, **22**, 323.
14 J. Mizusaki, H. Tagawa, T. Saito, T. Yamamura, K. Kamitani, K. Hirano, S. Ehara, T. Takagi, T. Hikita, M. Ippommatsu, S. Nakagawa and K. Hashimoto, *Solid State Ionics*, 1994, **70–71**, 52.
15 R. Radhakrishnan, A. V. Virkar and S. C. Singhal, *J. Electrochem. Soc.*, 2005, **152**, A927.
16 M. S. Schmidt, K. V. Hansen, K. Norrman and M. Mogensen, *Solid State Ionics*, 2008, **179**, 1436.
17 B. Fultz and J. M. Howe, *Transmisson Electron Microscopy and Diffractometry of Materials*, Springer, 2005.
18 W. S. Rasband, *ImageJ*, http://imagej.nih.gov/ij/, 2011.
19 M. W. Louie, M. Kislitsyn, K. Bhattacharya and S. M. Haile, *Solid State Ionics*, 2010, **181**, 173.
20 Y. K. Taninouchi, T. Uda, Y. Awakura, A. Ikeda and S. M. Haile, *J. Mater. Chem.*, 2007, **17**, 3182.
21 A. Ikeda and S. M. Haile, *Solid State Ionics*, 2011.
22 H. E. Swanson and E. Tatge, *National Bureau of Standards (U.S.), Circular*, 1953, **539**, 1.
23 A. Preisinger, K. Mereiter and W. Bronowska, *Mater. Sci. Forum*, 1994, **166**, 511.
24 E. Barsoukov and J. R. Macdonald, *Impedance Spectroscopy: Theory, Experiment, and Applications*, Wiley-Interscience, New York, 2005.
25 M. E. Orazem and B. Tribollet, *Electrochemical Impedance Spectroscopy*, Wiley-Interscience, New Jersey, 2008.
26 K. D. Kreuer, *J. Mol. Struct.*, 1988, **177**, 265.
27 Y. Fukai, *The Metal-Hydrogen System: Basic Bulk Properties*, Springer, 2005.
28 Y. Ebisuzak, W. J. Kass and M. Okeeffe, *J. Chem. Phys.*, 1968, **49**, 3329.
29 H. Katsuta and R. B. Mclellan, *J. Phys. Chem. Solids*, 1979, **40**, 697.
30 Y. Sakamoto and H. Kamohara, *J. Jpn. I. Met.*, 1981, **45**, 797.
31 E. Gileadi, M. A. Fullenwi and J. O. M. Bockris, *J. Electrochem. Soc.*, 1966, **113**, 926.
32 A. Varga, N. A. Brunelli, M. W. Louie, K. P. Giapis and S. M. Haile, *J. Mater. Chem.*, 2010, **20**, 6309.
33 K. A. Sasaki, Y. Hao and S. M. Haile, *Phys. Chem. Chem. Phys.*, 2009, **11**, 8349.
34 A. B. Papandrew, C. R. I. Chisholm, R. A. Elgammal, M. M. Ozer and S. K. Zecevic, *Chem. Mater.*, 2011, **23**, 1659.

